International Journal of Solids and Structures 282 (2023) 112451

Contents lists available at ScienceDirect

International Journal of Solids and Structures

journal homepage: www.elsevier.com/locate/ijsolstr

Mechanics of tubular meshes formed by elastic helical fibers

Jacopo Quaglierini [a], Marino Arroyo [b,c,d], Antonio DeSimone [a,e,*]

[a] The BioRobotics Institute, Scuola Superiore Sant'Anna, 56127 Pisa, Italy
[b] LaCàN, Universitat Politècnica de Catalunya-BarcelonaTech, Barcelona 08034, Spain
[c] Centre Internacional de Mètodes Numèrics en Enginyeria (CIMNE), 08034 Barcelona, Spain
[d] Institute for Bioengineering of Catalonia (IBEC), The Barcelona Institute for Science and Technology (BIST), 08028 Barcelona, Spain
[e] SISSA, 34136 Trieste, Italy

ARTICLE INFO

Keywords:
Braided mesh
Chebyshev nets
Helices
Envelope surface
Computational mechanics
Elastic rods

ABSTRACT

Tubular structures made of elastic helical fibers are widely found in nature and in technology. The complex and highly nonlinear mechanical properties of such assemblies have been understood either through minimal models or through complex simulations describing each individual fiber and their interactions. Here, inspired by Chebyshev's geometric model of nets, we propose and experimentally validate a modeling framework that treats tubular braided meshes as continuum surfaces corresponding to the virtual envelope defined by the fibers. The key idea is to relate surface geometry and fiber kinematics, enabling us to follow large deformations. This theory is amenable to efficient computations and, in axisymmetric cases, the problem reduces to finding two scalar fields defined over 1D segments. We validate our model against experiments of axial compression, revealing the existence of a plateau with vanishing stiffness in the axial force–displacement curve, a feature that could prove particularly useful in applications where an applied compressive force needs to be held constant even against settlements of the compressed object.

1. Introduction

Tubular structures made of elastic helical fibers are common in nature and technology. These structures appear in many different contexts at many different length scales and exhibit nontrivial mechanical properties. Examples are helices in the structures of folded proteins and biopolymers (*e.g.* , DNA, microtubules), the axoneme of eukaryotic flagella, helical fibers in the walls of plant cells and in muscular hydrostats, helical springs, braided composites, or antennas for space satellites (Chouaieb et al., 2006; Olson et al., 2013; Arroyo and DeSimone, 2014; Kuenstler et al., 2020; Gao et al., 2020; Quaglierini et al., 2021; Harte and Fleck, 2000a,b).

At intermediate scales, braided meshes in McKibben pneumatic actuators are an important example of tubular structures made of many interwoven helical fibers (Tondu, 2012; Hassan et al., 2018). These structures transform the radial expansion induced by inflating an inner balloon into axial displacements and exhibit a highly nonlinear, yet very robust and reproducible, mechanical response. Hence, they are particularly suitable for artificial muscle applications. Braided cylindrical meshes are also used as grippers following the principle of the Chinese finger trap (Shang et al., 2019). The large – yet fully reversible – deformations they exhibit in response to human and animal touch make the manipulation of these structures easy and rewarding. In fact, they are used as anti-stress devices for humans and as toys for kittens.

The highly nonlinear response stems from the variation of the geometry of the helical fibers as the structure is compressed or extended; for example, depending on the braiding angle of their fibers, they respond to pressurization by either extending or contracting along the axis. In applications where axial displacement is an undesired outcome of pressurization, as in reinforced garden hoses and tires, the fibers are wound at a special angle ("magic angle") for which no axial displacement is induced by variations of pressure. Furthermore, the axial stiffness of the mesh depends on the braiding angle, which is interesting as it makes the structure "adaptive", that is, its stiffness can be tuned by applying a compressive pre-load (Connolly et al., 2017).

To quantitatively understand the nonlinear mechanics of these assemblies, two different approaches of contrasting complexity have been followed. At one end, if any variation of the braiding angle along the axis is neglected and fibers are approximated as circular helices (Tondu, 2012), an application of the Principle of Virtual Work (PVW) defines a simple formula for the axial force necessary to balance a given internal pressure depending on the braiding angle. This modeling approach captures key features of these structures but it is too simplistic to faithfully reproduce many operating conditions of the braided devices.

* Corresponding author at: The BioRobotics Institute, Scuola Superiore Sant'Anna, 56127 Pisa, Italy.
E-mail address: antonio.desimone@santannapisa.it (A. DeSimone).

https://doi.org/10.1016/j.ijsolstr.2023.112451
Received 17 April 2023; Received in revised form 24 July 2023; Accepted 9 August 2023
Available online 11 August 2023

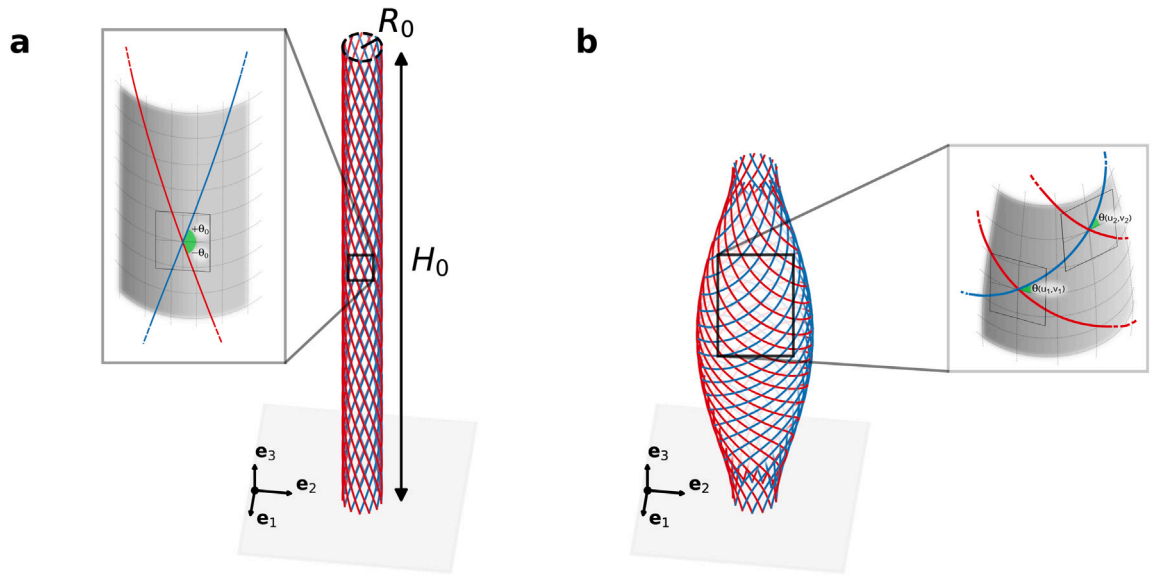

Fig. 1. (a) Sketch of the initial configuration of the mesh, with the initial braiding angle θ_0 highlighted in the inset. (b) Example of a deformed configuration of the mesh, where the braiding angle θ is a function of position.

At the other end, these structures have been modeled by an explicit "fiber-by-fiber" strategy using Finite Elements Methods (FEM); in this approach, fibers are divided into the truss-like elements that form the pantograph-like substructures of the mesh, which are then described and solved for as individual beams linked together through boundary conditions (Hassan et al., 2018). Despite their accuracy, these simulations are computationally expensive and do not reveal the inner working principles behind the overall behavior of these structures.

In this paper, we propose a new coarse-grained or mesoscopic modeling framework for tubular structures composed by helical fibers, formulated at an intermediate level of complexity, to retain the physical insight and computational efficiency of simple theories as well as the ability to quantitatively model complex non-uniform deformation scenarios. To this aim, we exploit the concept of virtual envelope surface, that is, the surface of revolution on which the center-lines of all fibers lie. The elastic energy of the envelope surface is then obtained from the energy stored by the deformed fibers, each modeled as a Kirchhoff rod, *i.e.*, as an inextensible and unshearable Cosserat rod. Similar approaches are found in Giorgio et al. (2015, 2016), Steigmann (2018b,a), Giorgio et al. (2018), Shirani and Steigmann (2021), McAvoy and Steigmann (2022). Considering axisymmetric deformations, our coarse-grained model reduces dramatically the complexity of the problem, which boils down to solving for two scalar fields, that is, the braiding angle θ that the fibers form with the parallels of the envelope surface as a function of their position along the axis of the tubular mesh, and the angle φ expressing the misalignment of the frame of directors with respect to the Darboux frame.

We then focus on the response under axisymmetric loads of cylindrical braided meshes, analyzing it through a computational implementation of our model, which we validate against experiments of axial compression. Our results highlight the existence of a plateau in the axial force/displacement curve, during which the mesh contracts under a constant compressive force with effectively zero stiffness (or "extreme compliance"), akin to superelasticity in shape-memory materials. However, rather than relying on the material microstructure and phase transformations at the atomic scale, here this response is the result of the architecture of the braid seen as a metamaterial. This remarkable feature could prove particularly useful in applications requiring force buffering against large extensions and compressions.

The remainder of this paper is organized as follows. In Section 2, we present the mathematical framework on which our model is based. In Section 3, we present our main findings on braided meshes and compare numerical simulations with experimental results. In Section 4, we discuss their implications and outline possible directions for future work.

2. Mathematical modeling

We consider a cylindrical mesh with initial radius R_0 and initial height H_0, composed of N_f identical inextensible fibers, whose center-lines form circular helices in the reference configuration, which we assume to be stress-free. Fibers are organized in pairs of helices of opposite chirality, *i.e.*, one right-handed and one left-handed, and share the same helical axis which coincides with the one of the mesh, see Fig. 1a. In the reference configuration, right-handed helices form a positive angle $\theta_0 \in (0, \pi/2)$ with the parallels of the cylinder (braiding angle), while left-handed ones form an angle equal to $-\theta_0$.

Our goal is to study equilibrium configurations of the mesh under compression or extension, while it is subjected to axisymmetric loads and constraints. To do so, we develop a continuum theory for the mesh based on its envelope surface, *i.e.*, the surface where the center-lines of the fibers lie. We then attribute the energy of the fibers, modeled as elastic Kirchhoff rods, to the envelope surface, thus reducing the complexity of the problem and speeding up its solution.

To obtain the kinematics of the envelope surface, we first describe it in the natural parametrization for surfaces of revolution in terms of parallels and meridians, both in reference and deformed configurations. Then, we impose the inextensibility of the fibers and obtain a formulation of the metric of the envelope surface in terms of θ, the angle that right-handed fibers form with the parallels of the mesh in the deformed configuration and that in principle depends on position (see Fig. 1b). By substituting the obtained metric into the natural parametrization, we describe the kinematics of the envelope surface in terms of θ alone. Finally, we model the fibers as Kirchhoff rods with an internal field φ, *i.e.*, the angle of misalignment of the frame of directors with respect to the Darboux frame of the rod as a curve embedded in the virtual envelope surface. The elastic energy of the mesh is then obtained in terms of the strains of the rods, that are functions of θ, φ. Note that we are assuming that no buckling occurs at the level of individual fibers. In fact, while single helical fibers tend to buckle under compression, it has been shown that meshes with a higher number of fibers ($N_f \geq 8$) are stabilized (Quaglierini et al., 2021).

2.1. Geometry and kinematics of the envelope surface as a surface of revolution

Let $\{e_1, e_2, e_3\}$ be the global Cartesian reference frame, with e_3 along the axis of the mesh. We describe the envelope surface of the mesh in its initial configuration as a cylinder, parametrized by

$$\chi_0(u,v) = \left(R_0 \cos\left(\frac{u}{R_0}\right), R_0 \sin\left(\frac{u}{R_0}\right), v \right), \quad (u,v) \in [0, L_0] \times [0, H_0],$$

where $L_0 = 2\pi R_0$. We restrict our attention to axisymmetric deformations, parametrized by

$$\chi(u,v) = \left(r(v)\cos\left(\frac{u}{R_0} + \psi(v)\right), r(v)\sin\left(\frac{u}{R_0} + \psi(v)\right), z(v) \right),$$

where $r(v), z(v)$ are the distance from the axis and the current axial coordinate, and $\psi(v)$ is the azimuthal displacement. We assume no sliding between fibers; since fibers are identical (modulo chirality) and both right-handed and left-handed ones are present, the system does not rotate with respect to its axis. Therefore, we set $\psi \equiv 0$,

$$\chi(u,v) = \left(r(v)\cos\left(\frac{u}{R_0}\right), r(v)\sin\left(\frac{u}{R_0}\right), z(v) \right).$$

For the sake of readability, we will drop the dependency from u, v in the following. We compute the columns of the derivative $\mathrm{D}\chi$ of the map χ,

$$\chi_{,u} = \left(-\frac{r}{R_0}\sin\left(\frac{u}{R_0}\right), \frac{r}{R_0}\cos\left(\frac{u}{R_0}\right), 0 \right),$$
$$\chi_{,v} = \left(r_{,v}\cos\left(\frac{u}{R_0}\right), r_{,v}\sin\left(\frac{u}{R_0}\right), z_{,v} \right),$$

where commas denote partial derivatives, and in turn the coefficients of the first fundamental form,

$$\begin{aligned} E &= \chi_{,u} \cdot \chi_{,u} = \left(\frac{r}{R_0}\right)^2, \\ F &= \chi_{,u} \cdot \chi_{,v} = 0, \\ G &= \chi_{,v} \cdot \chi_{,v} = (r_{,v})^2 + (z_{,v})^2. \end{aligned} \tag{1}$$

We then define a field of unit vectors normal to the surface,

$$\boldsymbol{N} := \frac{\chi_{,u} \wedge \chi_{,v}}{\|\chi_{,u} \wedge \chi_{,v}\|} = \frac{1}{\sqrt{G}} \left(z_{,v}\cos\left(\frac{u}{R_0}\right), z_{,v}\sin\left(\frac{u}{R_0}\right), -r_{,v} \right),$$

where $\{\chi_{,u}, \chi_{,v}, \boldsymbol{N}\}$ is a positively-oriented orthogonal basis of $\mathbb{R}^3$. Thus, the coefficients of the second fundamental form are computed as

$$\begin{aligned} e &= \chi_{,uu} \cdot \boldsymbol{N} = -\frac{r z_{,v}}{R_0^2 \sqrt{G}}, \\ f &= \chi_{,uv} \cdot \boldsymbol{N} = 0, \\ g &= \chi_{,vv} \cdot \boldsymbol{N} = \frac{r_{,vv} z_{,v} - r_{,v} z_{,vv}}{\sqrt{G}}. \end{aligned} \tag{2}$$

2.2. Angle-based parametrization of inextensible fibers

The braided mesh is composed of two families of non-orthogonal fibers. By definition, their center-lines lie on the envelope surface where, in the reference configuration, they form right-handed and left-handed helices with braiding angles θ_0, $-\theta_0$, respectively. Generic fibers, left- and right-handed, can be represented in the parametric plane u, v as

$$C^{\mathrm{L}}(s) = \left(u_0^{\mathrm{L}} + s\cos(\theta_0), H_0 - s\sin(\theta_0)\right), \qquad s \in \left[0,\ H_0 \sin^{-1}(\theta_0)\right], \tag{3}$$
$$C^{\mathrm{R}}(t) = \left(u_0^{\mathrm{R}} + t\cos(\theta_0), t\sin(\theta_0)\right), \qquad t \in \left[0,\ H_0 \sin^{-1}(\theta_0)\right], \tag{4}$$

where s, t are arc-length parameters and $u_0^{\mathrm{R}}, u_0^{\mathrm{L}}$ are u-intercepts of the two lines. The image of these parametric lines through the map χ_0, that is $\chi_0(C^{\mathrm{L}}(s))$, $\chi_0(C^{\mathrm{R}}(t))$, represents the center-lines of the fibers in the reference configuration; since χ_0 is an isometry, s, t are the arc-lengths of these space curves as well. After deformation, fibers are described

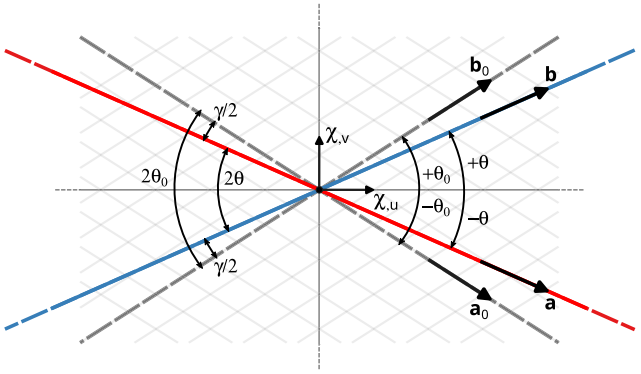

Fig. 2. Sketch of how the braiding angle changes during deformation, going from θ_0 to θ. The shear angle γ is also shown.

by $c^{\mathrm{L}}(s) = \chi(C^{\mathrm{L}}(s))$, $c^{\mathrm{R}}(t) = \chi(C^{\mathrm{R}}(t))$, with tangent vectors $\boldsymbol{a}(s) = c^{\mathrm{L}}_{,s}(s)$ and $\boldsymbol{b}(t) = c^{\mathrm{R}}_{,t}(t)$, computed by the chain-rule as

$$\boldsymbol{a} = [\mathrm{D}\chi](\cos(\theta_0), -\sin(\theta_0))^{\mathrm{T}} = \cos(\theta_0)\chi_{,u} - \sin(\theta_0)\chi_{,v}, \tag{5}$$
$$\boldsymbol{b} = [\mathrm{D}\chi](\cos(\theta_0), \sin(\theta_0))^{\mathrm{T}} = \cos(\theta_0)\chi_{,u} + \sin(\theta_0)\chi_{,v}. \tag{6}$$

To enforce the inextensibility of fibers, we impose that their tangent vectors remain of unit length, *i.e.*,

$$\boldsymbol{a} \cdot \boldsymbol{a} = \boldsymbol{b} \cdot \boldsymbol{b} = 1, \tag{7}$$

which, according to Eqs. (5),(6), is equivalent to

$$E\cos^2(\theta_0) + G\sin^2(\theta_0) = 1. \tag{8}$$

From the definition of $\theta(v) \in (0, \pi/2)$ as the current braiding angle, see Fig. 2, we have that

$$\boldsymbol{a} \cdot \boldsymbol{b} = \cos(2\theta), \quad \boldsymbol{a} \wedge \boldsymbol{b} = \sin(2\theta)\boldsymbol{N}. \tag{9}$$

Alternatively, we can compute the same quantities from Eqs. (5),(6) in terms of the metric induced by the deformation map,

$$\boldsymbol{a} \cdot \boldsymbol{b} = E\cos^2(\theta_0) - G\sin^2(\theta_0), \quad \boldsymbol{a} \wedge \boldsymbol{b} = (EG)^{\frac{1}{2}}\sin(2\theta_0)\boldsymbol{N}. \tag{10}$$

Hence, by combining Eqs. (8),(9),(10) we can rewrite E, G as

$$E = \frac{\cos^2(\theta)}{\cos^2(\theta_0)}, \quad G = \frac{\sin^2(\theta)}{\sin^2(\theta_0)}, \tag{11}$$

so that the metric tensor of the envelope surface of the mesh is a function of θ alone, *i.e.*,

$$g(\theta) = \begin{bmatrix} E & F \\ F & G \end{bmatrix} = \begin{bmatrix} \dfrac{\cos^2(\theta)}{\cos^2(\theta_0)} & 0 \\ 0 & \dfrac{\sin^2(\theta)}{\sin^2(\theta_0)} \end{bmatrix}. \tag{12}$$

Since fibers are inextensible, we can see the envelope surface of the braided mesh as *clothed/covered* by a Chebyshev net formed by the center-lines of our two families of fibers (Pipkin, 1984; Steigmann and Pipkin, 1991; Ghys, 2011; Baek et al., 2018) and, following previous classical work (Pipkin, 1984), we can define the shear angle γ as

$$\gamma = 2(\theta_0 - \theta), \tag{13}$$

where $\gamma > 0$ indicates a decrease of the internal angle between fibers (see Fig. 2). It can be shown that the well-known relations for Chebyshev nets hold in our case as well. In particular, we have that

$$\boldsymbol{b}_{,t} = \gamma_{,t}(\boldsymbol{b} \wedge \boldsymbol{N}) + (\boldsymbol{b}_{,t} \cdot \boldsymbol{N})\boldsymbol{N}, \tag{14}$$
$$K = \frac{\gamma_{,st}}{\sin(2\theta)}, \tag{15}$$

where K is the Gaussian curvature of the surface.

2.3. Geometry of the mesh in terms of the braiding angle

We have expressed the coefficients of the metric tensor in terms of $r(v), z(v)$, as well as in terms of the current braiding angle $\theta(v)$. By comparing Eqs. (1),(11) we obtain

$$r = \frac{R_0}{\cos(\theta_0)}\cos(\theta)\,, \qquad z_{,v} = \frac{\sin(\theta)}{\sin(\theta_0)}\left(1 - R_0^2\tan^2(\theta_0)\theta_{,v}^2\right)^{\frac{1}{2}}\,, \tag{16}$$

which we can substitute into Eq. (2) to get

$$\begin{aligned} e &= -\frac{r z_{,v}}{R_0^2\sqrt{G}} = -\frac{\tan(\theta_0)}{R_0}\frac{z_{,v}}{\tan(\theta)}\,,\\ g &= \frac{r_{,vv}z_{,v} - r_{,v}z_{,vv}}{\sqrt{G}} = -\frac{R_0}{\cos(\theta_0)\sin(\theta_0)}\sin^2(\theta)\frac{\theta_{,vv}}{z_{,v}}\,. \end{aligned} \tag{17}$$

Therefore, the geometry of the deformed envelope surface is fully described by its initial geometry and $\theta(v)$. Note that we assume $z_{,v} \geq 0$, thus excluding eversions of the mesh (local maxima of z). Moreover, the fact that the argument of the square root in Eq. (16) must be non-negative induces an embeddability constraint,

$$\theta_{,v}^2 \leq \frac{1}{R_0^2\tan^2(\theta_0)} \quad \Longleftrightarrow \quad -\frac{1}{R_0\tan(\theta_0)} \leq \theta_{,v} \leq \frac{1}{R_0\tan(\theta_0)},$$

showing that braiding angle distributions $\theta(v)$ with very large spatial variations cannot be achieved with an axisymmetric deformation map (Marder et al., 2007). Finally, according to the *Theorema Egregium* by Gauss, we can write the Gaussian curvature K in the (u, v) parametrization as

$$\begin{aligned} K &= -\frac{1}{2\sqrt{EG}}\left[\left(\frac{E_{,v}}{\sqrt{EG}}\right)_{,v} + \left(\frac{G_{,u}}{\sqrt{EG}}\right)_{,u}\right] =\\ &= -\frac{1}{2\sqrt{EG}}\left(\frac{E_{,v}}{\sqrt{EG}}\right)_{,v} = \frac{\sin^2(\theta_0)}{\cos(\theta)\sin(\theta)}\theta_{,vv}\,. \end{aligned} \tag{18}$$

While Eq. (15) is a well-known general result that holds true also for non-axisymmetric, non-tubular meshes, Eq. (18) is a special relation valid only for axisymmetric tubular nets, which in their reference configuration are cylinders with braiding angle θ_0 and axial coordinate v. However, this restricted formulation allows us to appreciate more directly how different angle profiles originate different geometries. In particular, it highlights that

1. $\theta \equiv const.$ leads to a cylinder:

$$\theta_{,v} \equiv 0 \quad \Rightarrow \quad r_{,v} = -\frac{R_0}{\cos(\theta_0)}\sin(\theta)\theta_{,v} \equiv 0\,,$$

2. $\theta = \alpha v$, $\alpha = const.$ leads to a cone:

$$\theta_{,v} \equiv \alpha \quad \Rightarrow \quad \frac{r_{,v}}{z_{,v}} = -\frac{\alpha R_0\tan(\theta_0)}{\left(1 - \alpha^2 R_0^2\tan^2(\theta_0)\right)^{\frac{1}{2}}} \equiv const\,,$$

3. $\theta_{,vv} \neq 0$ leads to surfaces with non-zero Gaussian curvature,

results that are not immediately apparent from the general formulation of Eq. (15). The results of the present section are analogous to those in Arroyo and DeSimone (2014) in the context of a different system of surfaces made of sliding rods.

2.4. Fibers as elastic Kirchhoff rods

Fibers are modeled as elastic Kirchhoff rods, with directors $\boldsymbol{d}_i^{\mathrm{R,L}}, i = 1,2,3$ forming a positively-oriented orthonormal basis at each point along them. Since we consider only axisymmetric deformations and fibers are mechanically equivalent, each fiber will have the same elastic energy regardless of its chirality, and the total elastic energy of the mesh will be the one of a single fiber times their number N_{f}, counting both right-handed and left-handed fibers. Therefore, in the following we will drop the superscripts R, L for the sake of readability, and we will study the kinematics of a single generic right-handed fiber.

Since the center-line of each fiber lies on the envelope surface, we can attach a second positively-oriented orthonormal frame to it, *i.e.*, the Darboux frame defined by $\{\boldsymbol{N}, (\boldsymbol{b}\wedge\boldsymbol{N}), \boldsymbol{b}\}$, where $\boldsymbol{b}$ is the tangent vector to the curve, and $\boldsymbol{N}$ is the vector normal to the surface. Under the Kirchhoff hypothesis, $\boldsymbol{d}_3$ coincides with $\boldsymbol{b}$, so that the two frames always share one vector. We can then express $\boldsymbol{d}_1$ in the Darboux frame as

$$\boldsymbol{d}_1 = \cos(\varphi)\boldsymbol{N} + \sin(\varphi)\,(\boldsymbol{b}\wedge\boldsymbol{N})\,, \quad \varphi \in [0, 2\pi),$$

and in turn

$$\boldsymbol{d}_2 = \boldsymbol{d}_3 \wedge \boldsymbol{d}_1 = \cos(\varphi)\,(\boldsymbol{b}\wedge\boldsymbol{N}) + \sin(\varphi)\boldsymbol{b}\wedge(\boldsymbol{b}\wedge\boldsymbol{N}) = \cos(\varphi)\,(\boldsymbol{b}\wedge\boldsymbol{N}) - \sin(\varphi)\boldsymbol{N}.$$

Summing up, the directors for a generic right-handed fiber with arc-length coordinate t are defined by

$$\begin{cases} \boldsymbol{d}_1(t) & := \cos(\varphi)\boldsymbol{N} + \sin(\varphi)\,(\boldsymbol{b}\wedge\boldsymbol{N})\,,\\ \boldsymbol{d}_2(t) & := \cos(\varphi)\,(\boldsymbol{b}\wedge\boldsymbol{N}) - \sin(\varphi)\boldsymbol{N}\,,\\ \boldsymbol{d}_3(t) & := \boldsymbol{b}\,. \end{cases}$$

Thus, we can describe the kinematics of fibers in terms of the one of the envelope surface – which in turn can be described in terms of $\theta(v)$ – and of the angle $\varphi(v)$. In the local basis $\{\boldsymbol{d}_1, \boldsymbol{d}_2, \boldsymbol{d}_3\}$, derivatives of directors along the fibers are expressed through the vector of strains $\boldsymbol{u} = (u_1, u_2, u_3)^{\mathsf{T}}$ (Antman, 2005; Goriely, 2017), that is,

$$\boldsymbol{d}_{i,t} = \boldsymbol{u}\wedge\boldsymbol{d}_i\,, \quad i = 1,2,3.$$

The strains are given by

$$\begin{cases} u_1 & = \boldsymbol{d}_{2,t}\cdot\boldsymbol{d}_3 = -\boldsymbol{d}_{3,t}\cdot\boldsymbol{d}_2 = \cos(\varphi)y_1 + \sin(\varphi)y_2\,,\\ u_2 & = \boldsymbol{d}_{3,t}\cdot\boldsymbol{d}_1 = -\boldsymbol{d}_{1,t}\cdot\boldsymbol{d}_3 = \cos(\varphi)y_2 - \sin(\varphi)y_1\,,\\ u_3 & = \boldsymbol{d}_{1,t}\cdot\boldsymbol{d}_2 = -\boldsymbol{d}_{2,t}\cdot\boldsymbol{d}_1 = y_3 + \sin(\theta_0)\varphi_{,v}\,, \end{cases} \tag{19}$$

where

$$y_1 = -\boldsymbol{b}_{,t}\cdot(\boldsymbol{b}\wedge\boldsymbol{N})\,, \quad y_2 = \boldsymbol{b}_{,t}\cdot\boldsymbol{N}\,, \quad y_3 = \boldsymbol{N}_{,t}\cdot(\boldsymbol{b}\wedge\boldsymbol{N})\,. \tag{20}$$

Since the rod kinematics depends on the shape of the envelope surface and on the angle between frames, strains can be expressed in terms of $\theta(v)$, $\varphi(v)$, and their derivatives. Next, we derive these relations. By recalling Eq. (9) and noting that

$$\boldsymbol{a}\cdot\boldsymbol{N}_{,t} = -\boldsymbol{a}_{,t}\cdot\boldsymbol{N}\,, \quad \boldsymbol{b}\cdot\boldsymbol{N}_{,t} = -\boldsymbol{b}_{,t}\cdot\boldsymbol{N},$$

we can rewrite y_3 as

$$\begin{aligned} y_3 &= \boldsymbol{N}_{,t}\cdot\left(\boldsymbol{b}\wedge\frac{(\boldsymbol{a}\wedge\boldsymbol{b})}{\sin(2\theta)}\right) = \boldsymbol{N}_{,t}\cdot\left(\frac{\boldsymbol{a}}{\sin(2\theta)} - \frac{\boldsymbol{b}}{\tan(2\theta)}\right) =\\ &= -\frac{\boldsymbol{a}_{,t}\cdot\boldsymbol{N}}{\sin(2\theta)} + \frac{\boldsymbol{b}_{,t}\cdot\boldsymbol{N}}{\tan(2\theta)}\,. \end{aligned} \tag{21}$$

From Eq. (6) we have

$$\boldsymbol{b}_{,t} = \cos^2(\theta_0)\chi_{,uu} + 2\cos(\theta_0)\sin(\theta_0)\chi_{,uv} + \sin^2(\theta_0)\chi_{,vv}\,, \tag{22}$$

$$\boldsymbol{a}_{,t} = \boldsymbol{b}_{,s} = \cos^2(\theta_0)\chi_{,uu} - \sin^2(\theta_0)\chi_{,vv}\,, \tag{23}$$

which combined with Eqs. (14),(21) allow us to rewrite Eq. (20) in terms of θ, z and their derivatives,

$$y_1 = -\gamma_{,t} = 2\sin(\theta_0)\theta_{,v}\,, \tag{24}$$

$$\begin{aligned} y_2 &= e\cos^2(\theta_0) + g\sin^2(\theta_0) =\\ &= -\frac{\cos(\theta_0)\sin(\theta_0)}{R_0}\frac{z_{,v}}{\tan(\theta)} - R_0\tan(\theta_0)\sin^2(\theta)\frac{\theta_{,vv}}{z_{,v}}\,, \end{aligned} \tag{25}$$

$$\begin{aligned} y_3 &= -\frac{e\cos^2(\theta_0) - g\sin^2(\theta_0)}{\sin(2\theta)} + \frac{e\cos^2(\theta_0) + g\sin^2(\theta_0)}{\tan(\theta)} =\\ &= -\tan(\theta)e\cos^2(\theta_0) + \frac{g\sin^2(\theta_0)}{\tan(\theta)} =\\ &= \frac{\cos(\theta_0)\sin(\theta_0)}{R_0}z_{,v} - \frac{R_0\tan(\theta_0)}{2}\sin(2\theta)\frac{\theta_{,vv}}{z_{,v}}\,. \end{aligned} \tag{26}$$

Recalling Eq. (16)$_2$, which expresses $z_{,v}(v)$ in terms of $\theta(v)$, we conclude that the strains $\boldsymbol{u} = (u_1, u_2, u_3)^\intercal$ given by Eq. (19) are functions of $\theta(v), \varphi(v)$ alone, *i.e.*,

$$u_i \equiv u_i\left(\theta(v),\, \theta_{,v}(v),\, \theta_{,vv}(v),\, \varphi(v),\, \varphi_{,v}(v)\right), \quad i = 1,2,3\,. \tag{27}$$

Notably, in the initial configuration we have $\theta \equiv \theta_0$, $\varphi \equiv 0$, which implies $z_{,v} \equiv 1$ and thus

$$u_{1\,0} = 0\,, \quad u_{2\,0} = -\frac{\cos^2(\theta_0)}{R_0}\,, \quad u_{3\,0} = \frac{\cos(\theta_0)\sin(\theta_0)}{R_0}\,. \tag{28}$$

Therefore, the bending strain $u_{2\,0}$ is equal in absolute value to the curvature of a circular helix and the torsional strain $u_{3\,0}$ is equal to the torsion of a right-handed circular helix(see Chapter 10.4 in Bower (2009)).

2.5. Energetics of the mesh

Let $W(u_1, u_2, u_3)$ be the elastic energy density of a single rod per unit length. Then, accounting for the fact that there are N_f rods in the assembly and that in the reference configuration the arc-length t of a rod is related to the parametric coordinate v by the relation $t = v/\sin\theta_0$, see Eq. (4), the elastic energy of the rod assembly can be written as

$$\mathcal{E}_\mathrm{el} := \frac{N_\mathrm{f}}{\sin\theta_0}\int_0^{H_0} W(u_1, u_2, u_3)\,\mathrm{d}v.$$

Recalling Eq. (27), it is clear that the elastic energy can be viewed as a functional of braiding angle and angle between rod and Darboux frames, $\mathcal{E}_\mathrm{el}[\theta, \varphi]$. The height of the mesh can be controlled by applying an axial force. The total potential energy accounting for the work of the axial force F is

$$\mathcal{E}[\theta, \varphi] = \mathcal{E}_\mathrm{el}[\theta, \varphi] - F\left(\int_0^{H_0} z_{,v}\,\mathrm{d}v - H_0\right). \tag{29}$$

Alternatively, the height of the mesh can be controlled introducing a constraint functional

$$\mathcal{E}[\theta, \varphi] = \mathcal{E}_\mathrm{el}[\theta, \varphi] - \lambda_\mathrm{h}\left(\int_0^{H_0} z_{,v}\,\mathrm{d}v - h_\mathrm{target}\right), \tag{30}$$

where λ_h is a Lagrange multiplier and h_target is the prescribed height of the mesh. To find the equilibrium configurations of the mesh, we use the Principle of Virtual Work, which requires that the functional $\mathcal{E}[\theta, \varphi]$ is stationary with respect to variations of its arguments, *i.e.*,

$$\delta\mathcal{E}\,(\theta, \varphi\,;\, \delta\theta, \delta\varphi) = 0\,, \quad \forall\delta\theta, \forall\delta\varphi,$$

where $\delta\mathcal{E}$ is the virtual variation of the total potential energy of the system under arbitrary virtual perturbations $\delta\theta, \delta\varphi$ of $\theta(v), \varphi(v)$ consistent with boundary conditions. We note that Eq. (16) expresses $r, z_{,v}$ in terms of θ, thereby providing the required relations to impose fixed position, Eq. (16)$_1$, or clamping boundary conditions, Eq. (16)$_2$. Boundary conditions may also constrain φ.

To model the elastic energy density of a single rod, we adopt a simple quadratic expansion given by

$$W(u_1, u_2, u_3) = \frac{1}{2}\left[B_1\left(u_1 - u_{1\,0}\right)^2 + B_2\left(u_2 - u_{2\,0}\right)^2 + B_3\left(u_3 - u_{3\,0}\right)^2\right],$$

where B_1, B_2 are bending stiffnesses of fibers along $\boldsymbol{d}_1, \boldsymbol{d}_2$, B_3 their torsional stiffness along $\boldsymbol{d}_3$; the intrinsic strains $u_{i\,0}$ are given by Eq. (28), so that the initial configuration is stress free.

The proposed theory is restricted to axisymmetry but otherwise is fully nonlinear and geometrically exact. The only additional assumption, that the rod center-lines of all symmetry-related rods remain on a virtual envelope surface, is purely kinematic and quite reasonable as further discussed in the next section. Hence, the only material parameters are the number of fibers, the initial braiding angle, and the elastic properties of the rods. It is interesting to note that it does not map to a usual membrane or shell theory, even an anisotropic one. Indeed, we can rewrite Eq. (24)–(26) as

$$y_1 = -\cos(\theta_0)\frac{E_{,v}}{\sqrt{EG}} = \tan(\theta_0)\sin(\theta_0)\frac{G_{,v}}{\sqrt{EG}}\,, \tag{31}$$

$$y_2 = e\cos^2(\theta_0) + g\sin^2(\theta_0)\,, \tag{32}$$

$$y_3 = \sin(\theta_0)\cos(\theta_0)\left(g\sqrt{\frac{E}{G}} - e\sqrt{\frac{G}{E}}\right), \tag{33}$$

showing that the elastic energy density of the surface depends not only on the first and second fundamental forms, as would a nonlinear Koiter shell theory, but also on derivatives of the metric coefficients. It can thus be interpreted as a nonlinear Koiter shell model with higher-order membrane elasticity. Furthermore, it depends on an additional internal field $\varphi(v)$.

2.6. Interweaving and sliding between fibers

In our model, all rods lie on the same virtual surface. If applied to braided interweaving fibers, our model makes an approximation since the non-interpenetrating fibers need to depart from this surface to interweave, which further results in cross-fiber interactions. In particular, additional elastic energy is stored because of interweaving (Peng et al., 2013). Indeed, at crossing points fibers interlace with one another and thus deviate from the behavior of circular helices. This local phenomenon can be seen as a "high-frequency oscillation" on their geometry, superimposed to the "low-frequency carrier" due to the curvature and torsion of the corresponding circular helix. By neglecting this effect, we are conceptually applying a "low-pass filter" to the kinematics of the braided mesh, thus discarding energy contributions from high-frequency contents. Moreover, another subtlety is represented by frictional interactions, whose complex nonlinear behavior is affected by the possibility that fibers slide with respect to each other. At least for now, we do not model these effects and neglect sliding between fibers. To ensure no inter-penetration, we constrain the braiding angle to remain between two limit values, *i.e.*, $\theta \in [\theta_\mathrm{min}, \theta_\mathrm{max}] \cap \left(0, \frac{\pi}{2}\right)$.

We remark that the realization of a surface made of two families of helical fibers is not restricted to braids. Our model can be physically realized with other micro-architectures such as pin-jointed rods (Olson et al., 2013).

3. Results

In order to validate our model, we study the behavior of a cylindrical mesh subjected to prescribed compression and we compare numerical results with experimental ones. We simulated two extreme cases for our model: in the first one, the misalignment angle φ is allowed to fully relax, while in the second one it is set to zero, effectively reducing our model to a one-parameter description. Since in this last scenario the frame of directors always coincides with the Darboux one, we shall refer to it as the "Darboux hypothesis".

3.1. Experimental setting

We used a commercial braided mesh with radius 4 mm, height 130 mm, made of 144 fibers. Fibers had an initial braiding angle of 71° and were 0.275 mm in diameter (measured with microscopy, see Fig. 3a); their ends are fused together so that no radial changes at the bases are allowed. In order to interface the mesh with an INSTRON® testing machine, we 3D-printed resin supports which work through friction. Once the mesh was mounted in place, its free length was 95 mm, see Fig. 3b.

The top base of the mesh was subjected to 7 cycle of prescribed axial displacements, in order to assess the magnitude of hysteresis in the system. At each cycle, the top base was lowered by 50 mm in 10 steps at 1 mm/s, with 5 s in between each ramp (to assess the magnitude

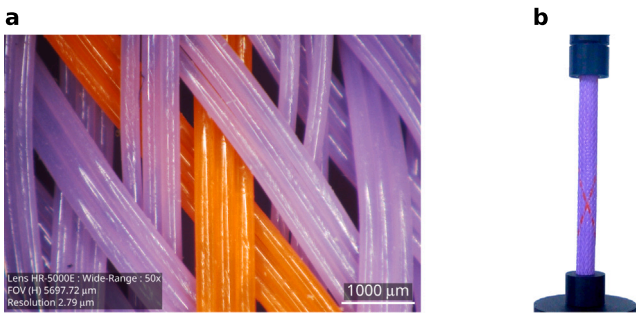

Fig. 3. (a) Microscopy of a fiber bundle (3D Digital Microscope HRX-01, Hirox). (b) The setup assembled and mounted in place.

of visco-elastic effects), and brought back to initial condition using the same timing of the loading steps. The axial force on the sample was measured using a 1-N load cell connected to the testing machine. Furthermore, the experiment was filmed to measure the braiding angle at a specific point of the mesh through image analysis, performed with a custom MATLAB® implementation of the Hough transform.

3.2. Numerical implementation

We implemented the previously described mathematical model with a MATLAB® custom code that solves for the equilibrium configuration of the structure by minimizing Eq. (30) with respect to $\theta(v), \varphi(v)$, discretized using a B-Spline approximation of degree 3. This approximation has differentiable second derivatives, and hence leads to square integrable elastic energies, which involve second derivatives of $\theta(v)$. The integrals in Eq. (30) are performed using a 3 point Gauss–Legendre quadrature rule. We solve the equilibrium problem numerically using a constrained optimization algorithm requiring the derivatives of the elastic energy and the length constraint with respect to the coefficients of the B-Spline expansions of $\theta(v)$ and $\varphi(v)$. We found that 43 degrees of freedom per field were enough for accurate results (that is, further refinements did not change the solutions), leading to fast simulations as detailed later.

We assumed that fibers have a circular cross-section, with diameter reported in Section 3.1. Furthermore, we set the following parameters:

1. initial braiding angle of the mesh $\theta_0 = 71°$, measured from microscopy images;
2. limit braiding angles $\theta_{\max} = \theta_0$ and $\theta_{\min} = 19°$, computed from image analysis;
3. number of fibers in the mesh $N_f = 144$, measured from the sample;
4. Young's modulus $E_Y = 4$ GPa and Poisson's ratio $\nu = 0.43$, that are reasonable values for plastic materials at room temperature;
5. bending stiffness $B_1 = B_2 \approx 1.123 \times 10^{-6}\,\mathrm{N\,m^2}$ and torsional stiffness $B_3 = B_1/(1+\nu) \approx 7.853 \times 10^{-7}\,\mathrm{N\,m^2}$, computed from the measured fiber diameter and E_Y assuming a circular cross-section.

We note that there are no additional parameters in our model, and hence no parameter was adjusted to fit experimental results.

We simulated the behavior of the mesh adopting a continuation approach, considering 41 levels of axial strain, from 0 up to $50/95 \approx 0.53$. The overall simulation took ≈ 4.71 seconds (MATLAB® R2022b on a Manjaro Linux distribution with RAM 64 GiB and processor Intel® Core™ i9-9900KFx16) solving for 86 degrees of freedom, compared to the $\sim 10^5$ of a typical FE model (Hassan et al., 2018).

3.3. Comparison of numerical and experimental force–displacement curves

We highlight two remarkable features of the mechanical response of the system, namely (1) the emergence of a broad plateau in the force–displacement curve (after a certain compression), see Fig. 4, and (2) the formation of a locked cylindrical region in the center of the mesh characterized by a limit angle, see Fig. 5a. Indeed, the axial force initially increases, so that the structure could be approximated as a linear spring in a regime of small compressions; the response then "softens" until the mesh reaches a flat region, *i.e.*, where small changes in θ do not affect the force experienced by the mesh. As compression further increases, a mechanical locked region between fibers nucleates at the center of the mesh as θ cannot be reduced below a limit angle; this angle is measured to be approximately equal to $90° - \theta_0$, and therefore set to this value in simulations. By further compressing the mesh, the angle θ reaches its limit value in a wider and wider region, forming a cylindrical core at the center of the structure (predicted also in Giorgio et al. (2018)). We notice that the force creep, occurring during pauses between loading steps, is small compared to the applied load, therefore justifying our treatment of the mesh as a purely elastic system.

From a quantitative point of view, the comparison between force–displacement curves, reported in Fig. 4, shows a good agreement between the experimental profile and the numerical one in the case $\varphi \equiv 0$ (Darboux hypothesis), while numerical results for fully relaxed φ tend to underestimate the compression force. A possible interpretation is that, in the real system, friction and interweaving between fibers hinders the relaxation of φ. In addition, Fig. 5b reports a comparison between the experimental angle-displacement profile and the numerical one from our simulations, both evaluated at $v \approx 0.36 H_0$ (*i.e.*, where the two red fibers cross). Overall, the profiles are close to one another, and the offset between them can be attributed to a systematic error introduced by the video setup.

Our model allows us to interpret the force plateau observed in experiments. In our simulations, the plateau region is characterized by a tangent modulus that decreases almost to zero compared with its initial value. This corresponds to an almost vanishing second derivative of the total energy with respect to the base displacement. In particular, the second derivative vanishes and even changes sign for simulations with unconstrained φ. This behavior can be described as an interplay of energetic components: while the second derivative of the torsional energy always remains positive, the ones of the bending energies progressively decrease and eventually become negative; once their magnitude is large enough to counterbalance the torsional component, the second derivative of the total elastic energy equals zero and thus the plateau emerges (see Fig. 6a). As soon as the locked region starts to appear, the second derivative of the total elastic energy increases back and the plateau ends.

3.4. Misalignment angle profiles

Regarding our simulation with unconstrained φ, Fig. 7 compares the initial configuration ($\varphi \equiv 0$) with the profiles of $\varphi(v)$ obtained at several displacements. For all configurations, the angle is anti-symmetric with respect to $v = H_0/2$, meaning that the director $\boldsymbol{d}_1$ coincides with the outer normal vector $\boldsymbol{N}$ at the ends and at the midpoint of the mesh. This was an expected feature: $\varphi(0)$, $\varphi(H_0) = 0$ and the problem is symmetric with respect the sagittal plane, so that the misalignment must be zero at $v = H_0/2$; moreover, in order to be symmetric with respect to the sagittal plane, $\boldsymbol{d}_1$ must deviate from $\boldsymbol{N}$ in opposite directions on the two halves of the mesh. The magnitude of the peaks in φ increases with the displacement, while their positions shift towards the ends of the mesh. While at lower compression levels the angle φ could be approximated with a sine, at sufficiently high ones it shows two lobes progressively closer to the ends of the mesh; in the central region, φ behaves almost linearly, with a slope at $v = H_0/2$ that decreases with compression.

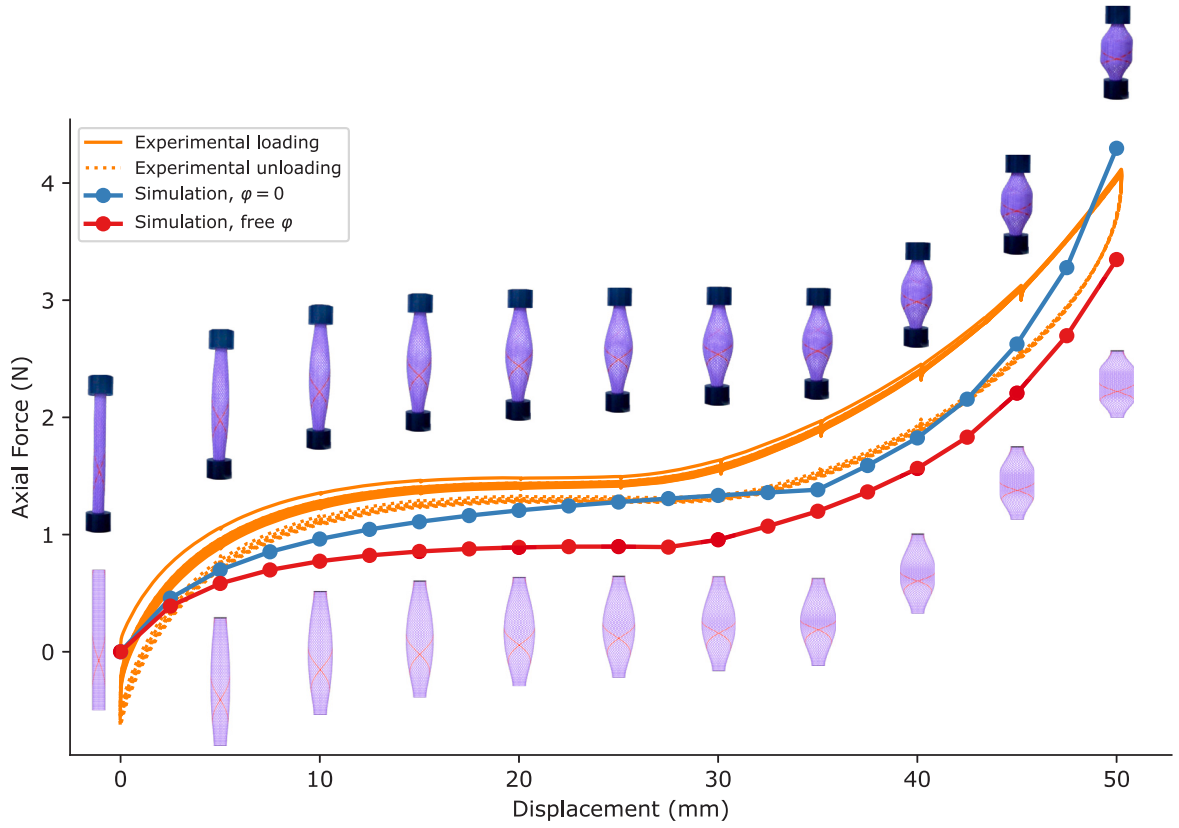

Fig. 4. Comparison between the force–displacement curves obtained through numerical simulations ($\varphi = 0$ and free φ) and the experimental one. Insets report equilibrium configurations at 11 compression levels, both for the experiment and the simulation with $\varphi = 0$..

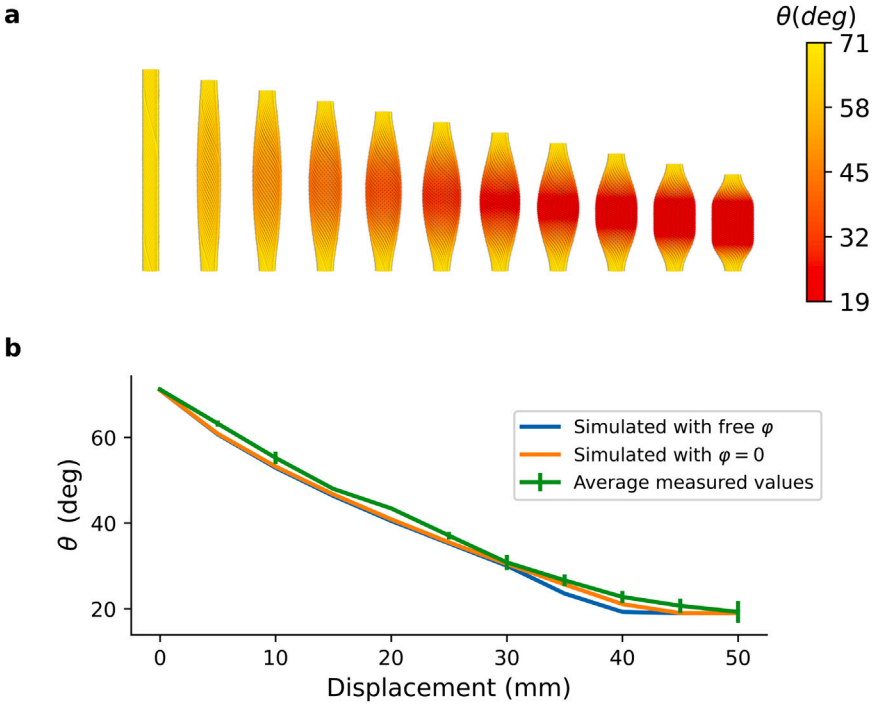

Fig. 5. (a) Evolution of the angle θ (in degrees) with increasing compressive displacements (case $\varphi = 0$). As compression increases, a locked cylindrical region, with $\theta = 90° - \theta_0 = 19°$, grows at the center of the mesh. (b) Comparison of numerical θ profiles, both for free φ and $\phi = 0$, with measured ones at $v \approx 0.36 H_0$. We reported the average of measurements across all cycles with bars indicating minimum and maximum measured values.

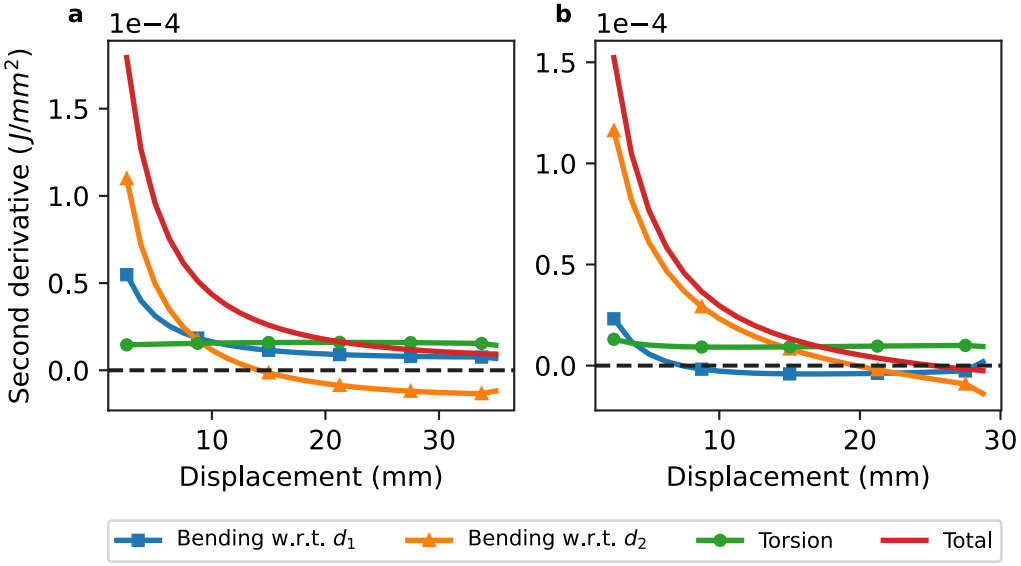

Fig. 6. Second derivative of bending, torsional, and total elastic energies of the mesh with respect to top-base displacements, in the case (a) $\varphi = 0$ and (b) unconstrained φ.

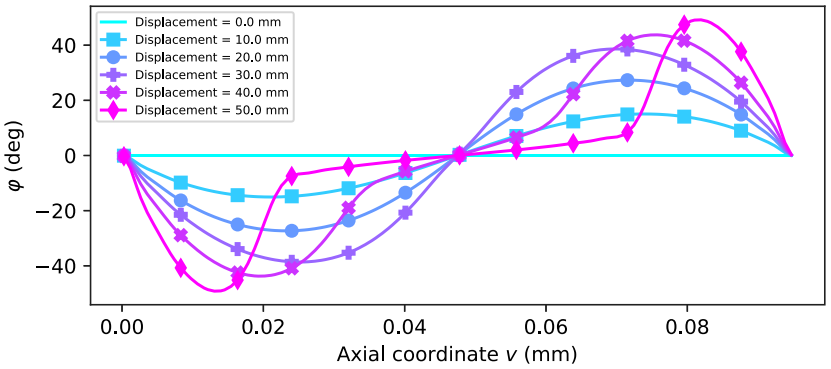

Fig. 7. Comparison of φ profiles for different compression levels. The angle can be initially approximated as a sine, while at higher compressions three zones emerge, that is, two lobes near the ends of the mesh and an almost linear region in the center .

This means that initially the central region stores energy through φ, and then releases it; remarkably, this happens at compression levels for which the central locked region has already started to arise.

Although no measures of this misalignment have been taken during experiments, the large peak values (more than 40°) that appear for unconstrained φ seem somehow unlikely, as they should lead to a visible macroscopic effect on the mesh. This fact, together with the fact that full relaxation of φ leads to underestimate the required compression force, see Fig. 4, suggests that, when braiding and friction are taken into account, the misalignment (if any) is reduced.

4. Discussion and conclusions

In conclusion, we developed an analytical model of a cylindrical braided mesh, implemented it numerically using B-Splines, and validated it against experimental observations. Results indicate that our model can predict the behavior of physical braided meshes with a good degree of accuracy and at low computational cost, which makes it suitable for design optimization through grid searches. In future work, we plan to extend our formulation in order to capture effects not modeled for the time being, such as friction, sliding, and interweaving of fibers. Also, it would be interesting to choose different models for the elastic energy of fibers, with energy densities growing with respect to the strains faster than quadratically.

We stress that the proposed model can capture the mechanical response of meshes under extension as well. However, extension tests are not feasible on commercial meshes: since they are typically wound at the angle of maximum packing ($\theta_0 \approx \theta_{max}$), their extension is limited to negligible displacements.

The emergence of the plateau region during compression experiments simultaneously poses interesting questions and opens new scenarios. Indeed, along the plateau, a braided mesh can compress an object with a force that remains constant even against settlements of said object. A deeper understanding of the phenomenon, that is, its dependency on geometric and material parameters as well as boundary conditions, could allow us to tune the plateau region, both in terms of its size and starting point, obtaining operating regions of "infinite" compliance. This feature will be investigated more closely in future work.

Declaration of competing interest

The authors declare that they have no conflict of interest.

Data availability

Data will be made available on request.

Acknowledgments

We thank G. Noselli for useful discussions on the plateau in the response under compression of braided tubular meshes, and for his help in manufacturing supports for the mesh. J.Q. and A.D.S. acknowledge the support of the Italian Ministry of University and Research (PRIN-2020PFCXPE) and of the European Union Horizon 2020 Research and Innovation Programme (I-Seed, Grant Agreement No101017940, MAPWORMS, Grant Agreement No101046846); M.A. acknowledges the support of the Generalitat de Catalunya (AGAUR: 2017-SGR-1278 and "ICREA Academia" award to M.A.), the European Research Council (CoG-681434 to M.A.). IBEC and CIMNE are recipients of a Severo Ochoa Award of Excellence from the MINECO. A.D.S is a member of the INDAM research group GNFM.

References

Antman, Stuart S., 2005. Problems in nonlinear elasticity. Nonlinear Probl. Elast. 513–584.

Arroyo, Marino, DeSimone, Antonio, 2014. Shape control of active surfaces inspired by the movement of euglenids. J. Mech. Phys. Solids 62, 99–112.

Baek, Changyeob, Sageman-Furnas, Andrew O., Jawed, Mohammad K., Reis, Pedro M., 2018. Form finding in elastic gridshells. Proc. Natl. Acad. Sci. 115 (1), 75–80.

Bower, Allan F., 2009. Applied Mechanics of Solids. CRC Press.

Chouaieb, Nadia, Goriely, Alain, Maddocks, John H., 2006. Helices. Proc. Natl. Acad. Sci. 103 (25), 9398–9403.

Connolly, Fionnuala, Walsh, Conor J., Bertoldi, Katia, 2017. Automatic design of fiber-reinforced soft actuators for trajectory matching. Proc. Natl. Acad. Sci. 114 (1), 51–56.

Gao, Tian, Siefert, Emmanuel, DeSimone, Antonio, Roman, Benoit, 2020. Shape programming by modulating actuation over hierarchical length scales. Adv. Mater. 32 (47), 2004515.

Ghys, Etienne, 2011. Sur la coupe des vetements. Variation autour d'un theme de Tchebychev. L'Enseignement Math. 57 (1), 165–208.

Giorgio, Ivan, Corte, Alessandro Della, dell'Isola, Francesco, Steigmann, David J., 2016. Buckling modes in pantographic lattices. C. R. Méc. 344 (7), 487–501. http://dx.doi.org/10.1016/j.crme.2016.02.009.

Giorgio, I., Dell'Isola, F., Steigmann, D.J., 2018. Axisymmetric deformations of a 2nd grade elastic cylinder. Mech. Res. Commun. 94, 45–48.

Giorgio, Ivan, Grygoruk, Roman, dell'Isola, Francesco, Steigmann, David J., 2015. Pattern formation in the three-dimensional deformations of fibered sheets. Mech. Res. Commun. 69, 164–171.

Goriely, Alain, 2017. The Mathematics and Mechanics of Biological Growth, Volume 45. Springer.

Harte, A.-M., Fleck, N.A., 2000a. Deformation and failure mechanisms of braided composite tubes in compression and torsion. Acta Mater. 48 (6), 1259–1271.

Harte, Anne-Marie, Fleck, Norman A., 2000b. On the mechanics of braided composites in tension. Eur. J. Mech. A Solids 19 (2), 259–275.

Hassan, Taimoor, Cianchetti, Matteo, Moatamedi, Moji, Mazzolai, Barbara, Laschi, Cecilia, Dario, Paolo, 2018. Finite-element modeling and design of a pneumatic braided muscle actuator with multifunctional capabilities. IEEE/ASME Trans. Mechatronics 24 (1), 109–119.

Kuenstler, Alexa S., Chen, Yuzhen, Bui, Phuong, Kim, Hyunki, DeSimone, Antonio, Jin, Lihua, Hayward, Ryan C., 2020. Blueprinting photothermal shape-morphing of liquid crystal elastomers. Adv. Mater. 32 (17), 2000609.

Marder, Michael, Deegan, Robert D., Sharon, Eran, 2007. Crumpling, buckling, and cracking: elasticity of thin sheets. Phys. Today 60 (2), 33.

McAvoy, R.C., Steigmann, D.J., 2022. Cosserat elasticity of helically wound cylinders. J. Elasticity http://dx.doi.org/10.1007/s10659-022-09934-z.

Olson, Gina, Pellegrino, Sergio, Banik, Jeremy, Costantine, Joseph, 2013. Deployable helical antennas for cubesats. In: 54th AIAA/ASME/ASCE/AHS/ASC Structures, Structural Dynamics, and Materials Conference. p. 1671.

Peng, Xiongqi, Guo, Zaoyang, Du, Tongliang, Yu, Woong-Ryeol, 2013. A simple anisotropic hyperelastic constitutive model for textile fabrics with application to forming simulation. Composites B 52, 275–281.

Pipkin, A.C., 1984. Equilibrium of Tchebychev nets. Arch. Ration. Mech. Anal. (ISSN: 1432-0673) 85 (1), 81–97. http://dx.doi.org/10.1007/BF00250867.

Quaglierini, Jacopo, Lucantonio, Alessandro, DeSimone, Antonio, 2021. Mechanics of tubular helical assemblies: ensemble response to axial compression and extension. Acta Mech. Sinica 37, 173–186.

Shang, Zufeng, Ma, Jiayao, Li, Jinhua, Zhang, Zemin, Zhang, Guokai, Wang, Shuxin, 2019. Self-forcing mechanism of the braided tube as a robotic gripper. J. Mech. Robotics 11 (5), 051002.

Shirani, M., Steigmann, D.J., 2021. Cosserat elasticity of lattice solids. J. Elasticity 151 (1), 73–88. http://dx.doi.org/10.1007/s10659-021-09859-z.

Steigmann, David J., 2018a. Continuum theory for elastic sheets formed by inextensible crossed elasticae. Int. J. Non-Linear Mech. 106, 324–329. http://dx.doi.org/10.1016/j.ijnonlinmec.2018.03.012.

Steigmann, DJ37729491408, 2018b. Equilibrium of elastic lattice shells. J. Eng. Math. 109, 47–61.

Steigmann, David J., Pipkin, Allen C., 1991. Equilibrium of elastic nets. Philos. Trans. R. Soc. Lond. Ser. A 335 (1639), 419–454.

Tondu, Bertr, 2012. Modelling of the McKibben artificial muscle: A review. J. Intell. Mater. Syst. Struct. 23 (3), 225–253.